

## Article

# Role of Hot Rolling in Microstructure and Texture Development of Strip Cast Non-Oriented Electrical Steel

Haitao Jiao <sup>1,2,3,\*</sup> , Xinxiang Xie <sup>2</sup>, Xinyi Hu <sup>2</sup>, Longzhi Zhao <sup>1,2,3,\*</sup>, Raja Devesh Kuma Misra <sup>4</sup>, Dejjia Liu <sup>2,3</sup>, Yanchuan Tang <sup>2,3</sup>  and Yong Hu <sup>2,3</sup>

- <sup>1</sup> Key Laboratory of Conveyance and Equipment, East China Jiaotong University, Ministry of Education, Nanchang 330013, China
- <sup>2</sup> School of Materials Science and Engineering, East China Jiaotong University, Nanchang 330013, China; xiexinxiang77@163.com (X.X.); hxy17370841144@163.com (X.H.); ldj515@126.com (D.L.); tangyanchuan89@163.com (Y.T.); huyong2136@163.com (Y.H.)
- <sup>3</sup> Key Laboratory of Advanced Materials for Vehicles & Laser Additive Manufacturing of Nanchang City, East China Jiaotong University, Nanchang 330013, China
- <sup>4</sup> Laboratory for Excellence in Advanced Steel Research, Department of Metallurgical, Materials, and Biomedical Engineering, University of Texas, El Paso, TX 79968, USA; dmisra2@utep.edu
- \* Correspondence: andrewjiao@163.com (H.J.); zhaolongzhi@163.com (L.Z.)

**Abstract:** In this study, the effect of the hot-cold rolling process on the evolution of the microstructure, texture and magnetic properties of strip-cast non-oriented electrical steel was investigated by introducing hot rolling with different reductions. The results indicate that hot rolling with an appropriate reduction, such as the 20% used in this study, increases the shear bands and {100} deformed microstructure in the cold roll sheet. As a result, in our study, enhanced  $\eta$  and Cube recrystallization texture and the improved magnetic induction were obtained. However, hot rolling with excessive reduction (36–52%) decreased the shear bands and increased the  $\alpha$ -oriented deformation microstructure with low stored energy. It enhanced the  $\alpha$  recrystallization texture and weakened the  $\eta$  texture, resulting in a decrease in the magnetic induction. In addition, hot rolling promoted the precipitation of supersaturated solid solution elements in the as-cast strip, thereby affecting the subsequent microstructure evolution and the optimization of its magnetic properties.

**Keywords:** non-oriented electrical steel; strip casting; microstructure; texture; magnetic properties



**Citation:** Jiao, H.; Xie, X.; Hu, X.; Zhao, L.; Misra, R.D.K.; Liu, D.; Tang, Y.; Hu, Y. Role of Hot Rolling in Microstructure and Texture Development of Strip Cast Non-Oriented Electrical Steel. *Metals* **2022**, *12*, 354. <https://doi.org/10.3390/met12020354>

Academic Editor: Marcello Cabibbo

Received: 22 January 2022

Accepted: 13 February 2022

Published: 18 February 2022

**Publisher's Note:** MDPI stays neutral with regard to jurisdictional claims in published maps and institutional affiliations.



**Copyright:** © 2022 by the authors. Licensee MDPI, Basel, Switzerland. This article is an open access article distributed under the terms and conditions of the Creative Commons Attribution (CC BY) license (<https://creativecommons.org/licenses/by/4.0/>).

## 1. Introduction

Non-oriented electrical steel (NOES) is an important soft magnetic metallic material for manufacturing motor cores and various electrical components. High magnetic induction and low iron loss are the two main performance requirements of NOES. The magnetic properties of NOES are not only affected by the content of (Si + Al) and thickness, but also by the grain size and crystallographic texture [1–4]. For products with a specific chemical composition, increasing the grain size reduces the hysteresis loss, but increases the eddy current loss and abnormal eddy loss [5]. This opposing change trend determines the existence of an optimum grain size for the lowest core loss. Obviously, this can be achieved by adjusting the annealing temperature and time. In addition, {100} texture ( $\langle 001 \rangle / \text{ND}$ ) is the ideal texture for high magnetic induction, since the easiest magnetization axis is  $\langle 001 \rangle$  in NOES with BCC (body-centered cubic) structure. However, the {100} texture is difficult to establish in the conventional processing route, which usually includes thick slab continuous casting, hot rolling, hot band annealing, cold rolling, and final annealing [6–8]. Complex orientation rotation and recrystallization behavior occur throughout thermomechanical processing and result in strong unfavorable  $\gamma$ -fiber ( $\langle 111 \rangle / \text{ND}$ ) and  $\alpha^*$ -fiber ( $\{11\ h\} \langle 1, 2, 1/h \rangle$ ) recrystallization textures [9,10]. Several special methods have been proposed to produce a {100} recrystallization texture [11–14].

In order to improve performance and reduce costs and energy consumption, steel companies are gradually exploring the preparation of NOES through a short-process technology. In recent years, the advanced short-process preparation technology of steel materials has mainly included CSP (compact strip production) and TRSC (twin-roll strip casting) [15,16]. In the CSP process, the molten steel is cast into a 50–70 mm thin slab and then directly rolled into a coil through a finishing mill. Compared with the conventional process, CSP has unique advantages in the preparation of NOES, such as uniform temperature distribution during hot rolling and the large grain size of the hot band [17]. NOES prepared by CSP has been significantly improved in terms of energy consumption reduction and magnetic properties [18], which is the main trend of current electrical steel production. Compared with CSP, TRSC technology is a significant breakthrough in the short-process preparation of steel. Strips with thicknesses of 1–5 mm can be directly produced and used for subsequent rolling and heat treatment. Here, the as-cast microstructure and the second phase particles can be precisely controlled based on the sub-rapid solidification process during TRSC [19,20]. In addition, element segregation is further suppressed, and the uniformity of the product is improved [21]. These characteristics of TRSC provide more opportunities for the microstructure and texture control of NOES. Studies indicate that strong Cube textures and high magnetic induction are easily obtained in NOES produced by TRSC and simple thermomechanical processing [22–24]. Therefore, it is the potential development direction for the manufacture of high-quality NOES in the future.

At present, the research on TRSC NOES mainly focuses on the influence of the as-cast microstructure and cold-rolling process on the magnetic properties [25–27]. The evolution and control of shear bands and {100} texture are the key subjects. In fact, the temperature of the as-cast strip after exiting the cast rollers still reaches over 1300 °C during strip casting. This feature provides good conditions for the on-line hot rolling of the strip. Furthermore, the reduction of hot rolling and cold rolling can be matched freely in TRSC process due to the thin strip, which enhances the controllability of the microstructure and the texture. However, there are limited studies on the effect of the hot-rolling process on the evolution of microstructure, as well as the recrystallization behavior and magnetic properties of NOES produced by TRSC. Therefore, in this study, a Fe-2.6%Si steel strip produced by TRSC was hot-rolled with different reductions, cold-rolled, and annealed. The role of hot rolling in the microstructural and textural development of TRSC NOES was clarified.

## 2. Materials and Methods

A Fe-2.6%Si-0.25%Al-0.1%Mn-0.005%S-0.007%N as-cast strip ~2.2 mm thick was produced by twin-roll strip casting process with superheat of ~40 °C. The raw materials were smelted in a vacuum furnace. After reaching the casting temperature, the molten steel was poured into a preheated tundish, and then poured into a molten pool composed of casting rollers and side dams. The casting speed was 26 m/min. Some 150 mm (RD, rolling direction) × 110 mm (TD, transverse direction) samples were cut from the air-cooled strip. Each sample was subjected to strip rolling, including hot rolling and cold rolling, as displayed in the schematic diagram (Figure 1). Four different rolling processes were designed to investigate the effect of the hot–cold rolling process on the microstructure and magnetic properties of strip-cast NOES. The processing parameters of different routes are listed in Table 1. Here, hot rolling with reductions of 36% and 52% was carried out in two and three passes with a strain rate of 2.3–3.3 s<sup>−1</sup>. All rolling process was carried out using a four-high rolling mill with work roller of 150 mm diameter, and the rolling speed was 0.06 m/s. Prior to hot rolling, the sample from the previous pass was heated to 1000 °C and held for 2 min in a box-type furnace. During the experiment, we noticed that the temperature of the thin strip sample dropped rapidly below 500 °C after only one pass of hot rolling. In order to implement multi-pass hot rolling, the sample from the previous pass was not cooled to room temperature and directly reheated to 1000 °C and held for 2 min between hot rolling passes. This process is different from conventional hot strip rolling because the strip is very thin in the TRSC line. This hot rolling process can be

performed by induction heating in industrial production. After hot rolling, the sample was pickled to remove the oxide scale and then cold-rolled to 0.50 mm, as shown in Table 1. Subsequently, the cold-rolled samples were subjected to the same annealing process in a  $N_2$  atmosphere. In addition, some samples cut from the cold-rolled sheet were annealed at 800 °C for different time and water-quenched to investigate the recrystallization process.

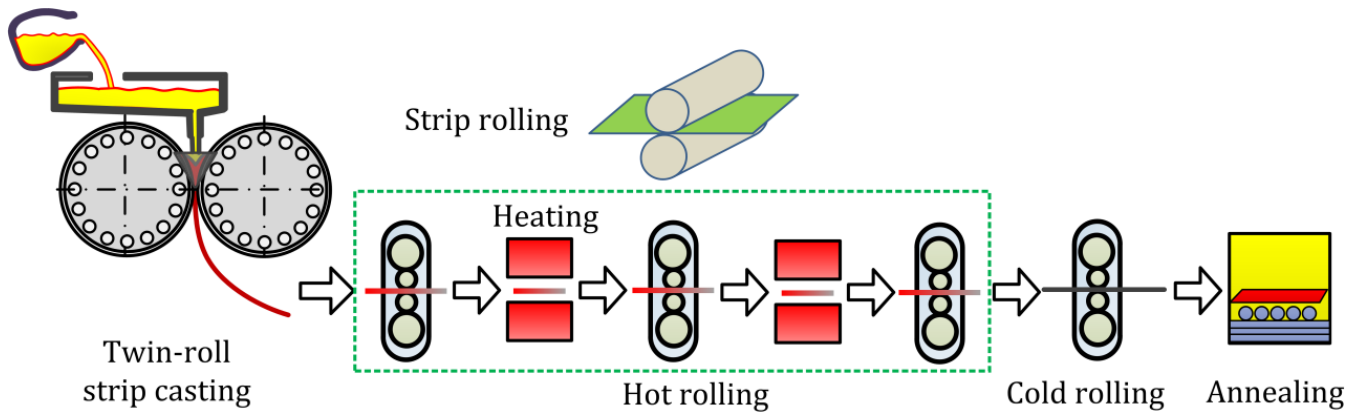


Figure 1. Schematic diagram of twin-roll strip casting, rolling, and annealing process.

Table 1. Processing parameters of the experimental non-oriented electrical steel.

Processing Route	Hot Rolling	Cold Rolling	Annealing
Route A	-	77% reduction (2.2→1.85→1.50→1.10→0.75→0.55→0.50)	1000 °C–6 min
Route B	20% reduction (2.2→1.75)	71% reduction (1.75→1.50→1.10→0.75→0.55→0.50)	1000 °C–6 min
Route C	36% reduction (2.2→1.75→1.40)	64% reduction (1.40→1.10→0.75→0.55→0.50)	1000 °C–6 min
Route D	52% reduction (2.2→1.75→1.40→1.05)	52% reduction (1.05→0.75→0.55→0.50)	1000 °C–6 min

The microstructure was characterized on an RD–ND (normal direction, ND) plane by an optical microscope after mechanical polishing and etching in 4% nital solution. Precipitate in the sample was observed by scanning electron microscope (SEM). The macrotexture of was measured on RD–TD plane by Bruker D8 Discover X-ray diffraction (XRD, Bruker, Billerica, MA, USA) with  $CoK\alpha_1$  radiation. The orientation distribution functions (ODFs) were calculated using TexTools software (version, Firefly Software LLC, Martinsburg, WV, USA) based on the {110}, {200}, and {211} incomplete pole figures obtained from XRD. The micro-texture of the microstructures was analyzed by electron backscatter diffraction (EBSD) equipped with the HKL technology Channel 5 software (Oxford Instruments, Abingdon, UK). Magnetic properties of annealed sheets of 100 mm length  $\times$  30 mm width were tested both along RD and TD by a MATS-2010M single sheet tester (Lianzhong Technology, Loudi, China). The magnetic induction  $B_{50}$  was determined at magnetic field strength of 5000 A/m, and the core loss  $P_{15/50}$  at 50 Hz was tested at magnetic flux density of 1.5 T. Three samples were measured in each direction and averaged.

### 3. Results and Discussion

#### 3.1. Microstructure and Texture of As-Cast and Hot-Rolled Strip

Figure 2 shows the microstructures of the as-cast and hot-rolled strips. The microstructure in the surface layer is mainly characterized by columnar grains, and the central layer is dominated by equiaxed grains (Figure 2a). The proportion of the columnar layer is more than 2/3 of the microstructure. The average grain size is  $\sim 245 \mu m$ . Here, the formation of columnar grains was associated with the large temperature gradient developed along the

normal direction induced by the rapid cooling of the cast roller [27], which promotes the preferential growth of grains. Compared with the surface layer, the temperature gradient in the central layer of the as-cast strip was lower. The formation of equiaxed crystals here may have been related to the flow of molten steel [28], which led to the melting and dissociation of dendrites that acted as the nuclei of the equiaxed grains. After hot rolling, the microstructure of the strip gradually refined. When the hot rolling reduction was 20%, several grains 30–50  $\mu\text{m}$  in size were observed at the surface layer (Figure 2b). Although dynamic recovery and dynamic recrystallization are important physical phenomena that occur during deformation at high temperature, dynamic recrystallization is difficult in BCC-structured electrical steel due to its high stacking fault energy [29–31]. Considering the low strain rate and rapid temperature drop during the hot rolling in this study, these small grains may originate from the inheritance of the as-cast microstructure. The central layer mainly suffered from plane strain compression with dynamic recovery, which resulted in flattened and elongated grains with few internal substructures. This is similar to the formation of hot-rolled microstructure in the conventional process and CSP process. When the hot rolling reduction reaches 36–52%, the microstructural difference between the surface and central layers is reduced (Figure 2c,d). The average grain size of these two samples decreased to  $\sim 167 \mu\text{m}$  and  $\sim 136 \mu\text{m}$ , respectively. In addition, the corrosion degree inside the deformed grains was light, indicating low stored energy [9]. Here, the change in microstructure was attributed to the static recrystallization during reheating process between hot rolling passes. In the case of 52% reduction by hot rolling, the hot-rolled sample underwent two recrystallization processes, so the grains were finer.

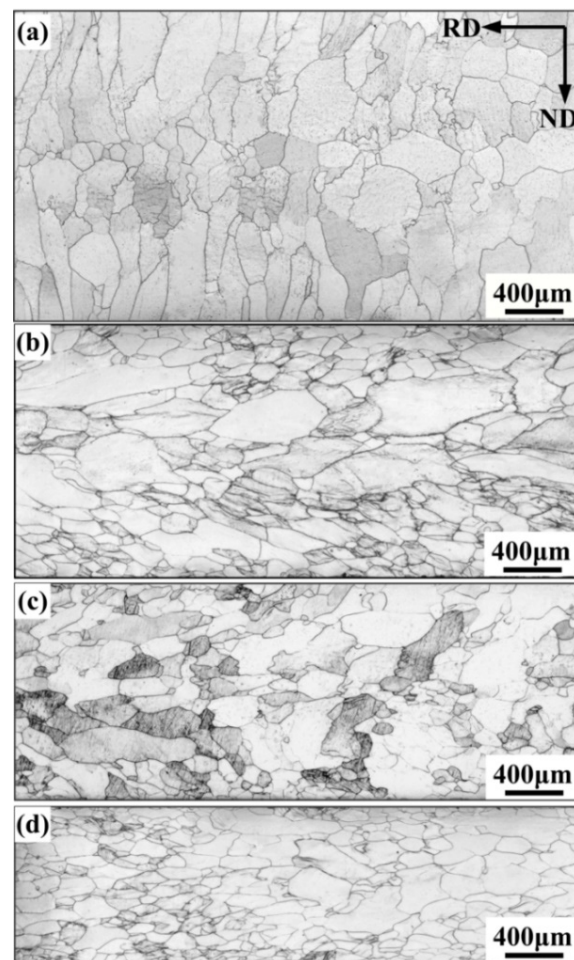


**Figure 2.** Microstructure of (a) as-cast Fe-2.8%Si strip and hot-rolled strip with reduction of (b) 20%, (c) 36%, and (d) 52%, respectively.

Figure 3 shows the macro-texture ( $\varphi_2 = 45^\circ$  ODF) of as-cast strip and hot-rolled strip with different reduction. The as-cast strip is characterized by strong  $\lambda$ -fiber texture, including all  $\{100\}$  components, with a peak at  $\{001\}\langle 120\rangle$ . After 20% hot rolling, the  $\lambda$ -fiber texture in the strip obviously weakened, and only exhibited  $\{001\}\langle 130\rangle$ - $\{001\}\langle 110\rangle$  components. A strong  $\alpha$ -fiber texture extending up to  $\sim 55^\circ$  along Euler angle  $\Phi$  and an  $\alpha^*$ -fiber texture extending up to  $\sim 25^\circ$  along Euler angle  $\Phi$  developed in the hot-rolled strip. The peak texture was located at ( $\varphi_1 = 15^\circ$ ,  $\Phi = 12^\circ$ ,  $\varphi_2 = 45^\circ$ ), with a  $\sim 8^\circ$  deviation from the  $\{114\}\langle 841\rangle$  orientation. In addition, a weak Goss texture was observed. When the hot-rolling reduction reached 36%, the  $\lambda$ -fiber texture was weakened further. The  $\{001\}\langle 110\rangle$  and  $\{001\}\langle 130\rangle$  components were still present. The texture was dominated by  $\alpha$ -fiber and  $\alpha^*$ -fiber texture. Compared with 20% hot rolling, the components of  $\alpha$ -fiber texture reduced, and the peak shifted from  $\{001\}\langle 110\rangle$  to  $\{117\}\langle 110\rangle$  ( $\varphi_1 = 0^\circ$ ,  $\Phi = 10^\circ$ ,  $\varphi_2 = 45^\circ$ ). When the hot-rolling reduction further increased to 52%, the  $\alpha$  and  $\alpha^*$  deformation textures significantly weakened. The peak texture was located at a  $\{118\}\langle 441\rangle$  orientation with a  $\sim 10^\circ$  deviation from the  $\{001\}\langle 110\rangle$  orientation. It was also noted that some  $\{332\}\langle 113\rangle$  ( $\varphi_1 = 90^\circ$ ,  $\Phi = 65^\circ$ ,  $\varphi_2 = 45^\circ$ ) components developed in the 36–52% hot-rolled strips.

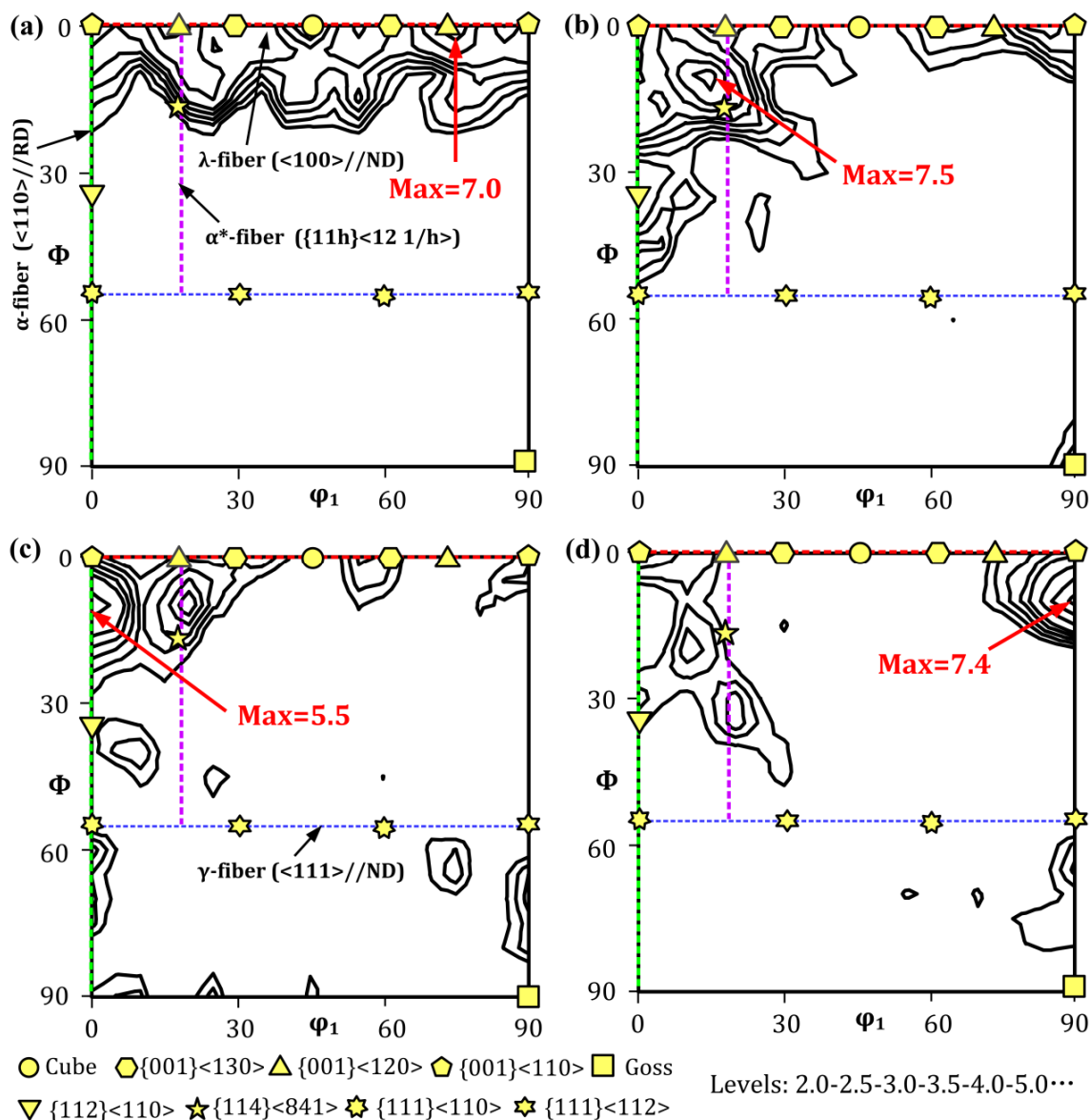
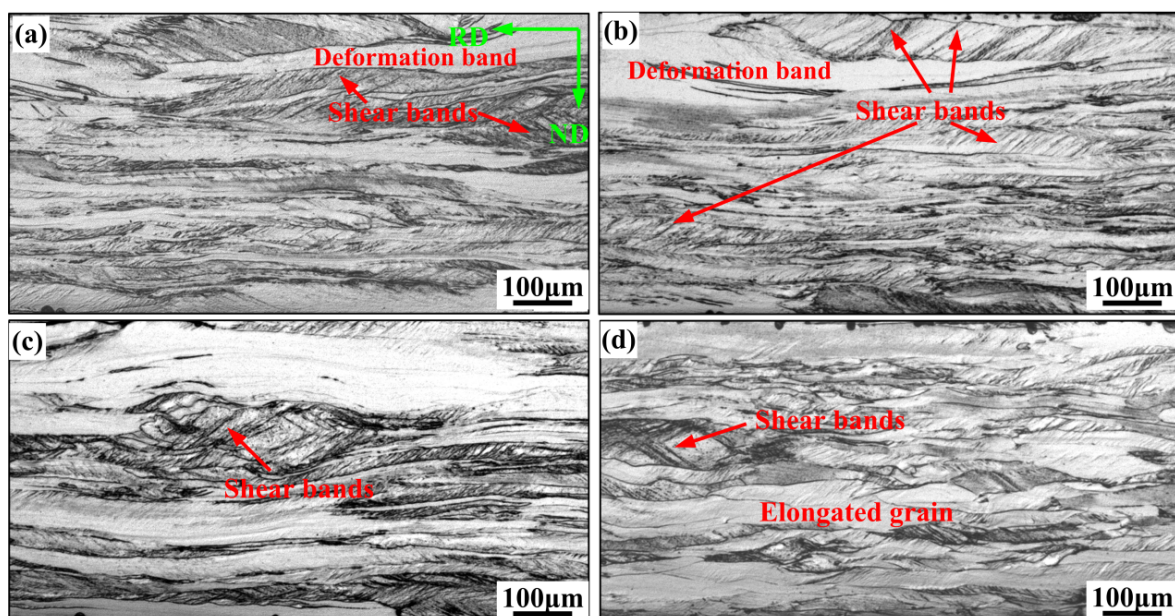


Figure 3. Macro-texture ( $\varphi_2 = 45^\circ$  ODFs) of (a) as-cast strip and hot-rolled strip with reductions of (b) 20%, (c) 36%, and (d) 52%, respectively.

The above results indicate that hot rolling significantly weakens the {100} texture in the as-cast strip, which is different from the effect of cold rolling reported in a previous study [32]. It is likely that {100} was enhanced in the case of direct cold rolling due to the formation of new Cube deformation bands in the {115}<051>-{115}<161> grains [32]. Hot rolling at high temperature destroys this behavior due to the change in slip system and deformation resistance. In addition, unlike the conventional process and the CSP process, the strip should be reheated for multi-pass hot rolling in the TRSC process because of the rapid temperature drop. In this case, static recrystallization during the reheating of the hot-rolled strip changed the deformation texture. This may have been the reason for the weakened  $\alpha$ -fiber and  $\alpha^*$ -fiber deformation texture in the hot-rolled strip with 36–52% reduction.

### 3.2. Cold-Rolled Microstructure and Texture

The cold-rolled microstructure of the strip subjected to different hot-rolling process is illustrated in Figure 4. A light etched area with deformation bands and a dark etched area with internal shear bands were identified in all the samples. The deformation stored energy generally increased with the increase in corrosion degree [9]. In the case of direct cold rolling, the grains fragmented severely together with the occurrence of a large number of shear bands (Figure 4a). Shear banding is a characteristic feature of plastic instability caused by the local concentration of imposed strain [33]. The development of shear bands is related to factors such as strain, deformation temperature, and initial grain size. In this study, the large reduction during direct cold rolling was favorable for the formation of shear bands, which may be destroyed during the subsequent continuous flattening of the grains. After the introduction of 20% hot rolling, the degree of grain flattening in the cold-rolled microstructure reduced, and the number and length of shear bands increased slightly (Figure 4b). This was probably because the recovery during hot rolling relieved the strain concentration and delayed the appearance of shear bands during the subsequent cold rolling. At this point, the established shear bands were less destroyed. When 36% hot rolling was introduced, the deformation bands in the cold-rolled sheet increased, while the shear bands decreased. When the hot rolling reduction reached 52%, the degree of grain fragmentation significantly reduced. Only a few shear bands were observed, and the stored energy of the overall deformed microstructure was low. This was related to the enhancement of recovery during hot rolling and the decrease in the cold-rolling reduction.



**Figure 4.** Cold-rolled microstructure of sheet subjected to (a) processing route A, (b) route B, (c) route C, and (d) route D, respectively.

Figure 5 shows the macro-texture of the cold-rolled sheet subjected to different processing routes. The orientation intensities along the  $\alpha$ -fiber,  $\gamma$ -fiber, and  $\lambda$ -fiber are displayed in Figure 6. In the case of direct cold rolling (Route A), the cold-rolled texture was characterized by strong  $\alpha$ -fibers including  $\{001\}\langle 110\rangle$ - $\{223\}\langle 110\rangle$  ( $\varphi_1 = 0^\circ$ ,  $\Phi = 43^\circ$ ,  $\varphi_2 = 45^\circ$ ) components, and strong  $\{100\}$  components from  $\{001\}\langle 110\rangle$  to  $\{001\}\langle 120\rangle$ . The peak texture was located at  $\{001\}\langle 110\rangle$  with intensity  $f(g) = 16.3$ . After introducing hot rolling with 20% reduction (Route B), the texture was dominated by strong  $\alpha$ -fiber and  $\lambda$ -fiber and weak  $\{111\}\langle 112\rangle$  texture. Compared with direct cold rolling, the intensity of  $\{001\}\langle 110\rangle$ - $\{114\}\langle 110\rangle$  components in the  $\alpha$ -fiber texture decreased, while the intensity of  $\{113\}\langle 110\rangle$ - $\{223\}\langle 110\rangle$  increased. In the  $\lambda$ -fiber texture, the intensity of  $\{001\}\langle 110\rangle$ - $\{001\}\langle 120\rangle$  decreased and the intensity of  $\{001\}\langle 130\rangle$ —Cube increased. When the hot-rolling reduction reached 36–52%, the  $\alpha$  cold-rolling texture gradually concentrated to a  $\{112\}\langle 110\rangle$  orientation. The  $\lambda$ -fiber texture gradually weakened, while the  $\gamma$ -fiber texture was enhanced.

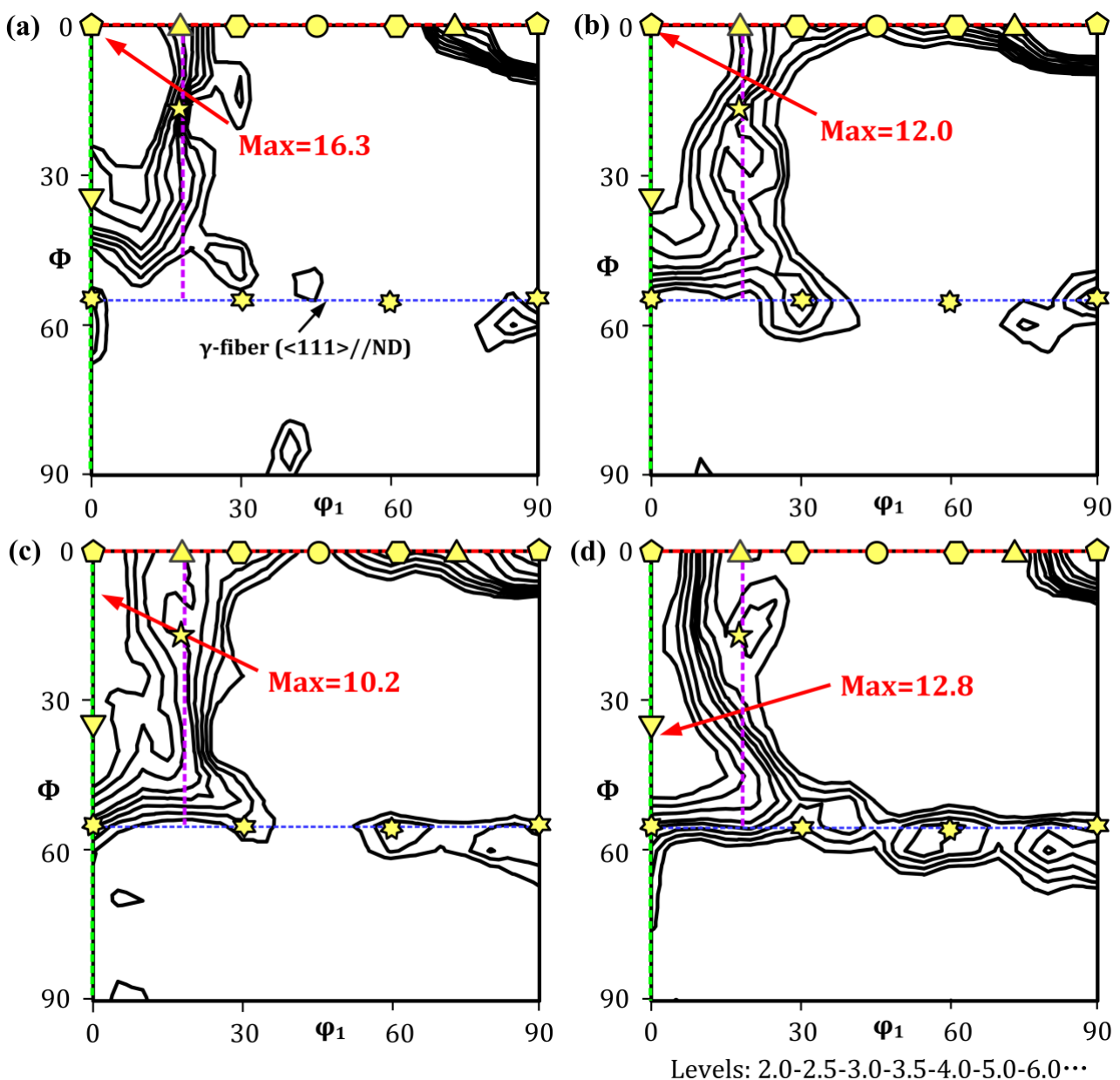


**Figure 5.** Macro-texture ( $\varphi_2 = 45^\circ$  ODFs) of cold-rolled sheet subjected to (a) processing route A, (b) route B, (c) route C, and (d) route D, respectively.

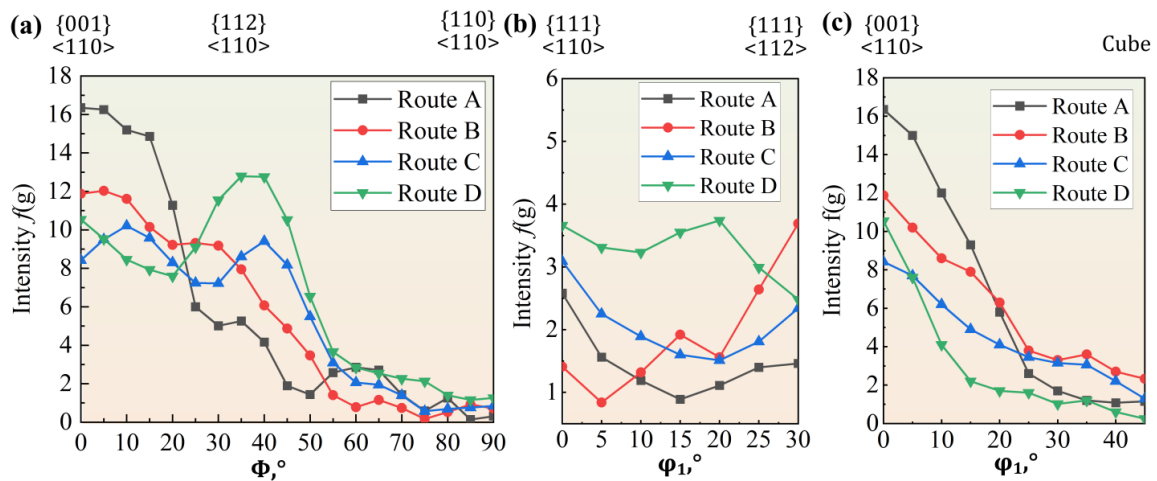


**Figure 6.** Orientation intensities along (a)  $\alpha$ -fiber, (b)  $\gamma$ -fiber, and (c)  $\lambda$ -fiber textures in cold-rolled sheet subjected to different processing routes.

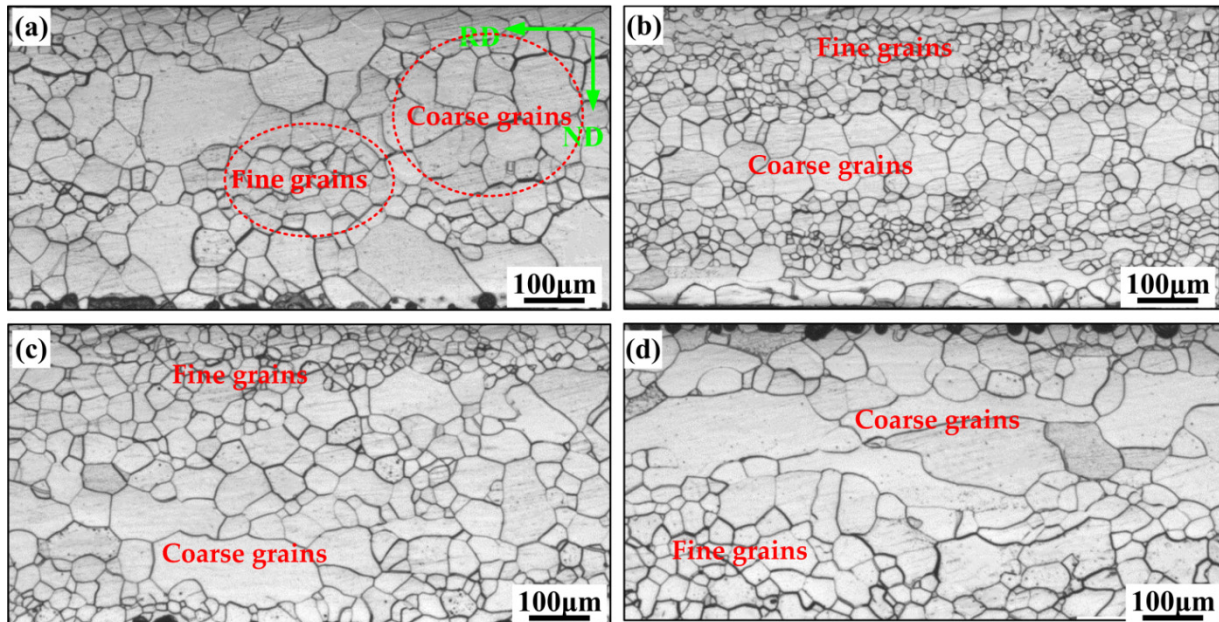
Orientation rotation is a typical feature of crystal deformation produced by the dislocation slip. According to the rotation path in BCC electrical steel reported previously [32], the  $\{100\}$  orientation tends to rotate to  $\{001\} \langle 110 \rangle$  around the ND axis and further to the  $\alpha$ -fiber texture around the RD axis. Hot rolling at high temperature will retard the localized strain concentration due to dynamic recovery. Therefore, crystal rotation was delayed, thereby enhancing the inheritance of  $\{100\}$  texture in the sample subjected to 20% reduction by hot rolling. On the other hand, the appearance of the  $\{111\} \langle 112 \rangle$  cold rolling texture was attributed to the rotation of the Goss and  $\{332\} \langle 113 \rangle$  texture developed during hot rolling. When multi-pass hot rolling was introduced (Routes C and D), the occurrence of recrystallization destroyed some favorable orientation rotation behaviors, such as  $\{115\} \langle 051 \rangle$  and  $\{115\} \langle 161 \rangle$  rotating to Cube orientation. As a result, the  $\{100\}$  deformation texture weakened. In addition, the  $\{332\} \langle 113 \rangle$  texture during hot rolling rotated to  $\{111\} \langle 112 \rangle \rightarrow \{111\} \langle 110 \rangle \rightarrow \{223\} \langle 110 \rangle$ , resulting in the enhancement of the  $\gamma$  and  $\alpha$  textures.

### 3.3. Recrystallization Microstructure and Texture

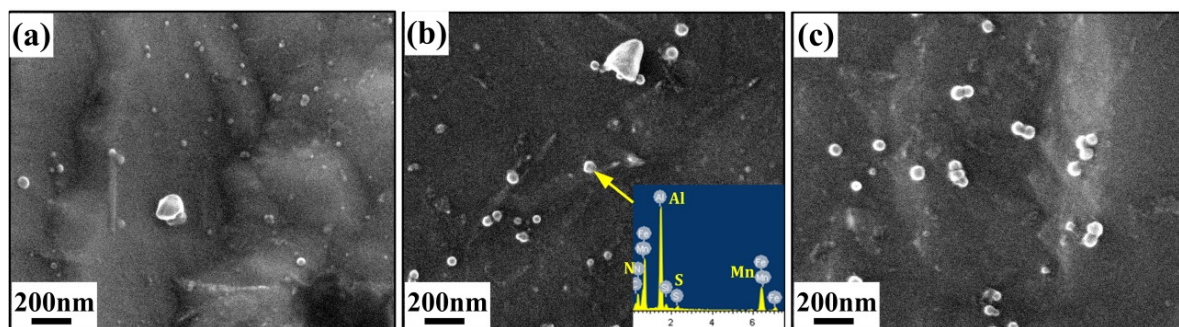
Figure 7 illustrates the typical recrystallized microstructure of the annealed sheet subjected to different rolling processes. Fine-grain colonies and coarse-grain colonies were identified in the inhomogeneous microstructure. The development of fine grains was attributed to the recrystallization of the shear bands or transition bands with high stored energy. Compared to the sample after direct cold rolling, the average grain size of the recrystallized microstructure subjected to 20% reduction hot rolling decreased from  $\sim 34 \mu\text{m}$  to  $\sim 22 \mu\text{m}$ . With the increase in the hot-rolling reduction, the average grain size of the annealed microstructure increased to  $\sim 29 \mu\text{m}$  in sample C and  $\sim 37 \mu\text{m}$  in sample D, respectively.

Changes in recrystallized microstructures are related to dislocation density and precipitates. The introduction of hot rolling decreases the dislocation density in the final cold-rolled microstructure. As a result, the nucleation rate of recrystallization is reduced, which generally leads to an increase in the size of the recrystallized grains. However, in this study, the elements in the as-cast strip were in a supersaturated solid-solution state due to the rapid solidification during strip casting. After direct cold rolling and annealing, AlN-MnS precipitates size 20–30 nm on size were formed, as shown in Figure 8a. These precipitates inhibited the growth of recrystallized grains through the grain boundary pinning effect. The introduction of hot rolling provided the thermodynamic and kinetic conditions for the precipitation of these particles in advance. As a result, the size of the AlN-MnS particles in the final annealed sheet increased to 30–60 nm (Figure 8b). According

to Jenkins [34], these particles have a stronger pinning effect, thereby decreasing the grain size. As the hot-rolling reduction reached 36–52%, the effect of the reduced nucleation rate on recrystallization gradually exceeded the pinning effect of the second-phase particles, resulting in an increase in the grain size.



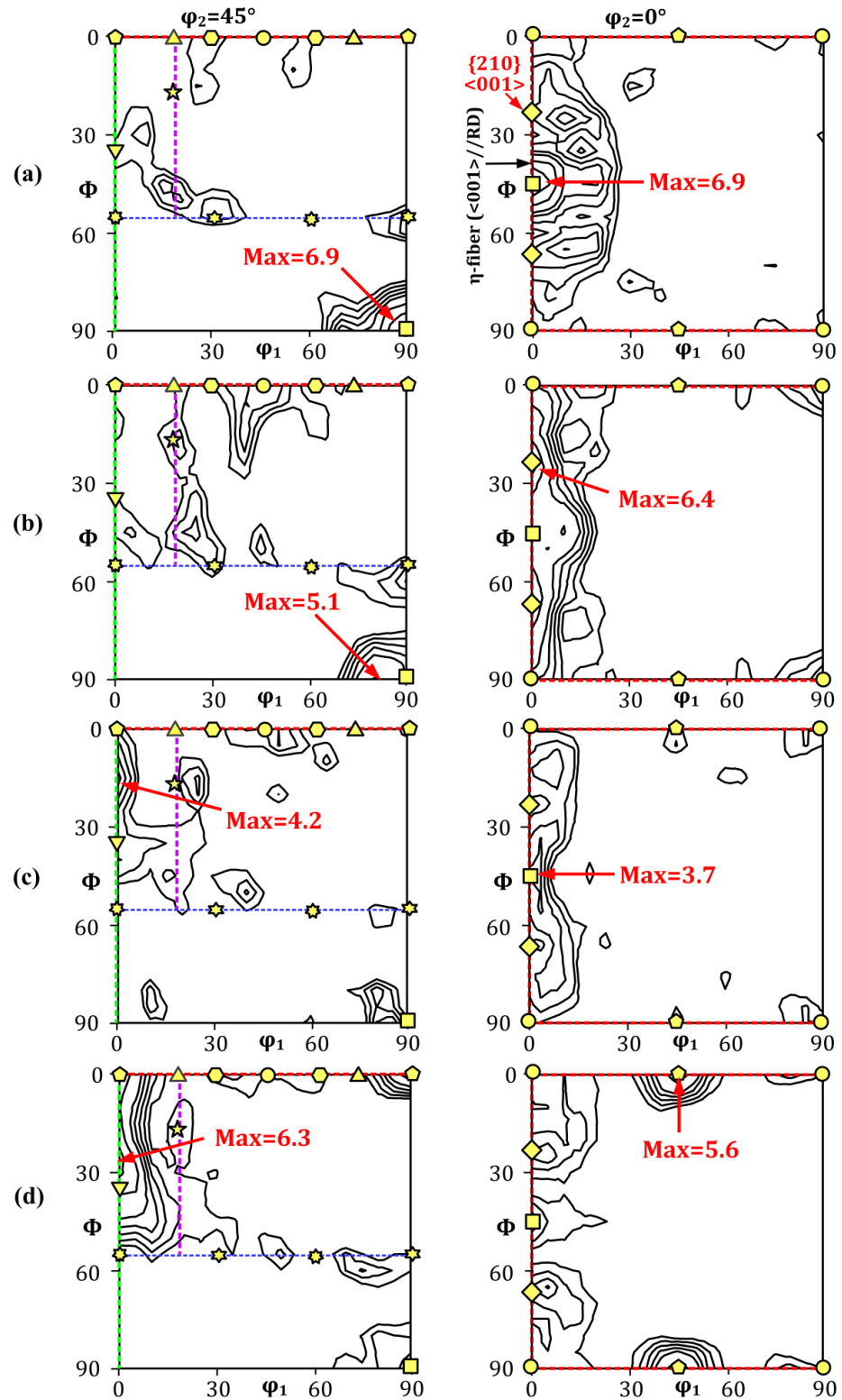
**Figure 7.** Recrystallized microstructure of sheet subjected to different hot-rolling and cold-rolling process: (a) route A by direct cold rolling; (b) route B by 20% reduction hot rolling; (c) route B by 36% reduction hot rolling; (d) route B by 52% reduction hot rolling.



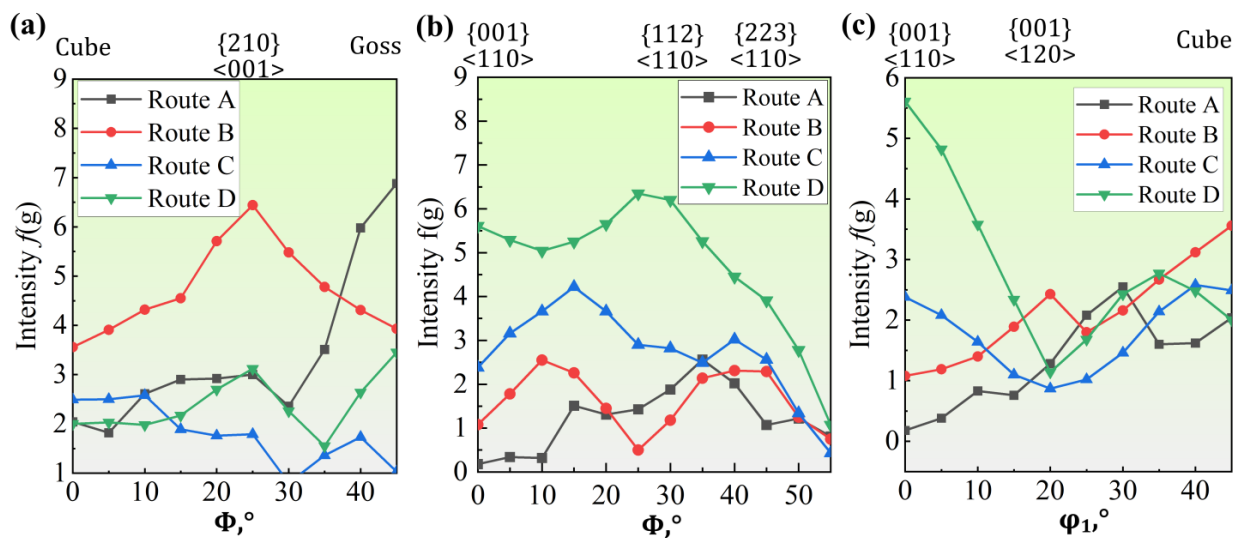
**Figure 8.** Precipitates in the final annealed micro-structure: (a) sample processed by route A; (b) sample processed by route B; (c) sample processed by route D.

Figure 9 shows the recrystallization texture of the final annealed sheet subjected to different rolling processes. The intensity of the specific texture components is shown in Figure 10. Sample A, processed by direct rolling, exhibited a strong  $\eta$ -fiber ( $\langle 001 \rangle // \text{RD}$ ) texture with peaks at Goss and  $\{210\}\langle 001 \rangle$ . In addition, weak  $\{111\}\langle 112 \rangle$  and  $\{001\}\langle 130 \rangle$  components developed. Sample B, subjected to 20% reduction hot rolling, was also characterized by weak  $\{111\}\langle 112 \rangle$  components and strong  $\eta$ -fiber textures with a peak at  $\{120\}\langle 001 \rangle$ . Compared to sample A, the other components of the  $\eta$ -fiber texture were enhanced, with the exception of Goss orientation. Furthermore, relatively strong Cube components and weak  $\alpha^*$ -fiber textures, such as  $\{114\}\langle 841 \rangle$ , were observed. For sample C, with 36% reduction hot rolling, the  $\eta$ -fiber texture and  $\lambda$ -fiber texture were obviously weakened. The recrystallization texture was dominated by pronounced  $\{115\}\langle 110 \rangle$ , one  $\alpha$ -fiber component. When 52% reduction hot rolling was adopted, the recrystallization texture of sample D displayed strong  $\alpha$ -fiber textures, including  $\{00\}\langle 110 \rangle$ - $\{223\}\langle 110 \rangle$  components.

The intensities of the  $\eta$ -fiber texture and the  $\{100\}$  texture decreased further. Therefore, hot rolling with an appropriate reduction (such as the 20% used in this study) enhances the  $\eta$ -fiber and  $\lambda$ -fiber recrystallization texture. However, an excessive reduction in hot rolling weakens both textures and leads to the formation of strong  $\alpha$ -fiber recrystallization textures.



**Figure 9.** Recrystallization texture ( $\varphi_2 = 45^\circ$  and  $\varphi_2 = 0^\circ$  ODFs) of sheet subjected to different processing routes: (a) route A; (b) route B; (c) route C; (d) route D.



**Figure 10.** Intensity of specific texture components in the annealed samples subjected to different rolling processes: (a)  $\eta$ -fiber; (b)  $\alpha$ -fiber; and (c)  $\lambda$ -fiber texture.

Changes in recrystallization texture are related to changes in deformed micro-structure and texture. Figure 11 illustrates the orientation image maps of partially recrystallized micro-structures in a sample subjected to different processing routes. When direct cold rolling was adopted (Route A), there were many shear bands in the deformed micro-structure (Figure 4), which provided nucleation sites for the  $\eta$ -fiber texture dominated by Goss and  $\{210\}\langle 001\rangle$  (Figure 11a). Moreover, these components recrystallized quickly due to their high stored energy, thereby rapidly swallowing the surrounding matrix, and developed as the main recrystallization texture. As 20% reduction by hot rolling was introduced, the increase in the number and length of shear bands in the cold-rolled microstructure enhanced the recrystallization behavior of the  $\eta$ -fiber oriented grains (Figure 11b). In addition, the  $\{100\}$  components increased in the cold-rolled sheet (Figure 5), which can enhance  $\{100\}$  annealing textures through normal recrystallization or extended recovery [30]. However, when the hot-rolling reduction increased to 36–52%, the decrease in shear bands in the cold-rolled sheet weakened the nucleation of the  $\eta$ -fiber and  $\lambda$ -fiber oriented grains (Figure 11c). At the same time, the  $\alpha$ -deformed microstructure with low stored energy increased. These grains recrystallize slowly and may form new  $\alpha$ -oriented grains through extended recovery. Thus, strong  $\alpha$ -fiber textures and weak  $\eta$ -fiber textures were developed.

### 3.4. Magnetic Properties

The magnetic properties of the annealed sheet are shown in Figure 12. The magnetic induction  $B_{50}$  at RD and TD of sample A processed by direct cold rolling was  $\sim 1.74$  T and  $\sim 1.67$  T, respectively. The  $B_{50}$  at RD of sample B processed by 20% reduction hot rolling increased to  $\sim 1.76$  T, while the value at TD was almost unchanged. For samples C and D, which experienced hot rolling with reductions of 36–52%, the  $B_{50}$  at both RD and TD decreased gradually. The average value of the two was lower than that of sample A without hot rolling. For the core loss, the  $P_{15/50}$  value of sample B was the highest. As the hot-rolling reduction increased, the  $P_{15/50}$  gradually decreased. However, compared with sample A, the maximum decrease in the average  $P_{15/50}$  was only  $\sim 0.1$  W/kg.

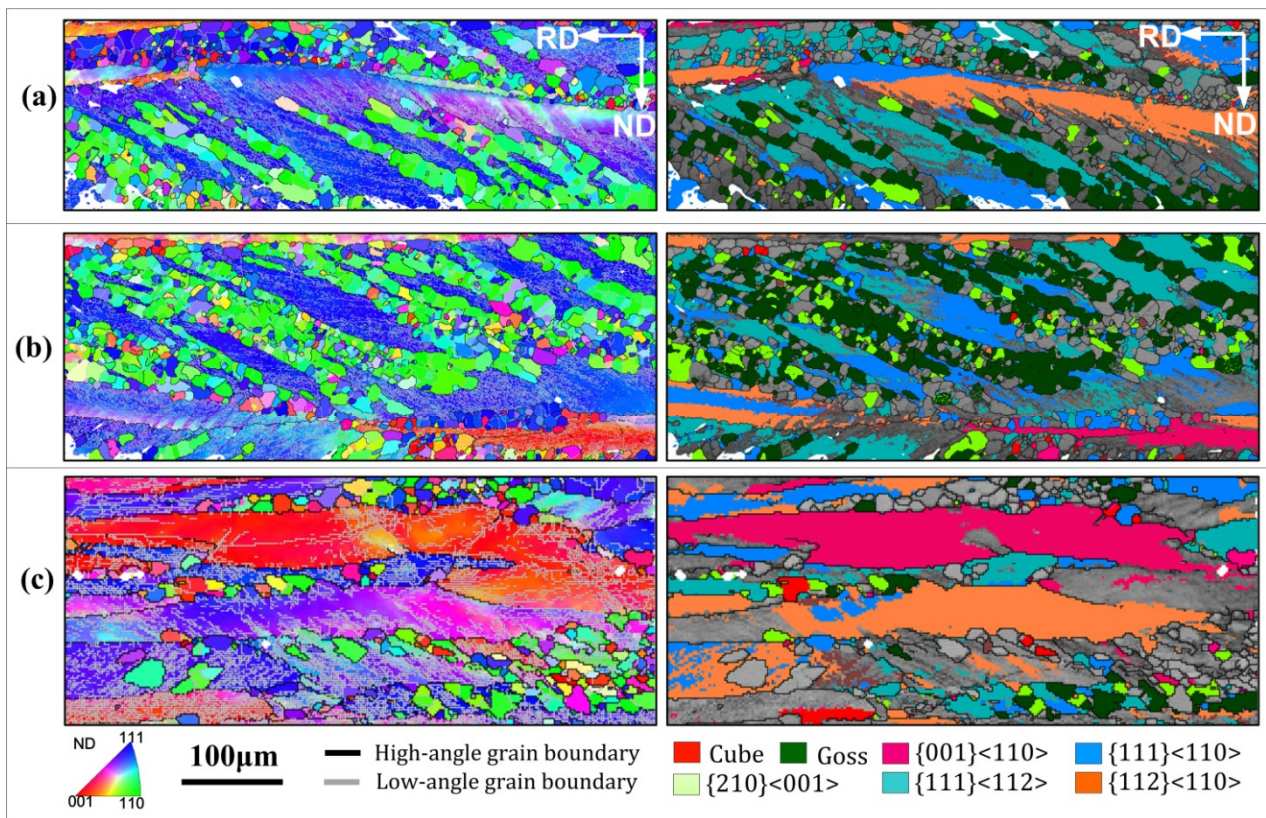


**Figure 11.** EBSD inverse pole figure (IPF) map and orientation distribution image (OIM) of partially recrystallized microstructure: (a) sample processed by route A; (b) sample processed by route B; (c) sample processed by route D.

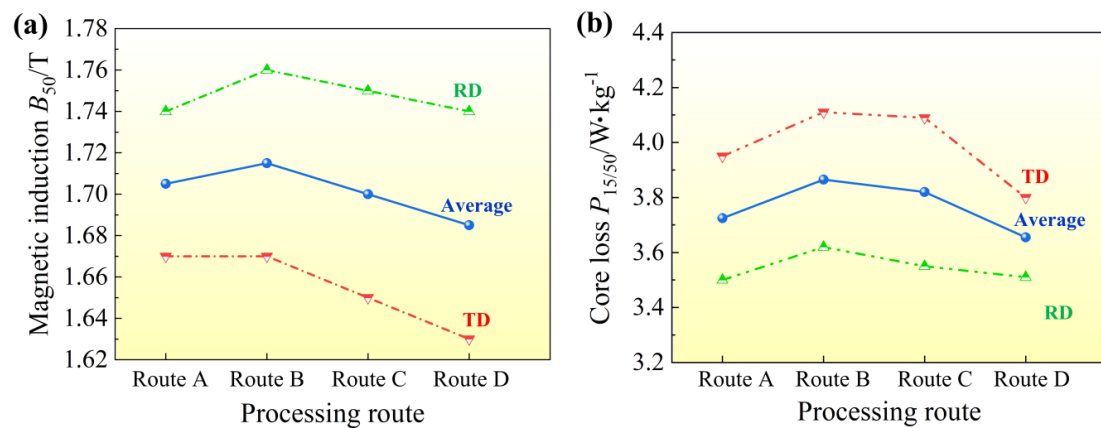


**Figure 12.** Magnetic properties of annealed sheet subjected to different processing routes: (a) magnetic induction  $B_{50}$ ; (b) core loss  $P_{15/50}$ .

The magnetic induction of non-oriented steel is mainly dependent on crystallographic texture [2]. It is well known that  $\langle 001 \rangle$  is the easy magnetization axis and  $\langle 111 \rangle$  is the hard magnetization axis. In the case of direct cold rolling (sample A), the strong  $\eta$ -fiber recrystallization texture induced high magnetic induction at RD because its  $\langle 001 \rangle$  axis was parallel to RD. However, the  $\langle 110 \rangle$  axes of the Goss and  $\{111\}\langle 112 \rangle$  textures were parallel to TD, resulting in low magnetic induction at TD. When hot rolling with 20% reduction was performed (sample B), the enhanced  $\eta$ -fiber and Cube recrystallization texture with  $\langle 001 \rangle // RD$  increased the magnetic induction at RD. When the hot-rolling reduction increased to 36–52% (samples C and D), the decreased magnetic induction at

both RD and TD was attributed to the weakening of the favorable  $\eta$ -fiber texture and the enhancement of the unfavorable  $\alpha$ -fiber texture. For the core loss, the main part of total loss at the low-frequency application of 50 Hz is the hysteresis loss, which was mainly affected by the grain size in this study [3]. The increased grain size decreases the area of the domain walls and the hysteresis loss. For the sample subjected to 20% reduction hot rolling, the grain size in the annealed sample was obviously reduced, which increased the hysteresis loss and the total core loss. As the hot-rolling reduction increased, the average grain size of the final annealed sheet increased. Here, the coarse-grained regions in the inhomogeneous microstructure had faster local domain wall movement than the fine-grained regions. As a result, the core loss decreased. However, the grain size difference between samples A, B, C, and D was small, so the core loss changed slightly. In conclusion, appropriate hot rolling and cold rolling are beneficial for enhancing favorable textures and improving magnetic induction. However, the introduction of hot rolling affects the precipitation behavior of second-phase particles, which in turn affects the grain size and iron loss, and needs to be further optimized.

#### 4. Conclusions

Non-oriented electrical steel prepared by twin-roll strip casting was processed by hot rolling and cold rolling with different reductions. The effect of the hot-cold rolling process on the microstructure, texture, and magnetic properties was investigated. The main results are summarized as follows.

- (1) The microstructure deformed by direct cold rolling exhibited many shear bands, strong  $\alpha$ -fibers, and  $\{001\}\langle 110\rangle$ - $\{001\}\langle 120\rangle$  texture. The introduction of hot rolling with 20% reduction increased the number and width of shear bands in the cold-rolled sheet, but larger reductions (36% and 52%) reduced the shear bands and the stored energy. This was because the recovery during the hot rolling and the static recrystallization during the reheating relieved the local strain concentration. With the increase in hot-rolling reduction, the  $\gamma$  and  $\alpha$  textures in the cold-rolled sheet were enhanced, which was related to the static recrystallization process during reheating and orientation rotation behavior.
- (2) Compared to direct cold rolling, the grain size of the final annealed sheet decreased after adopting 20% reduction hot rolling. This was attributed to the formation of AlN-MnS precipitates 30–60 nm in size with a strong grain boundary pinning effect. With the increase in hot-rolling reduction, the grain size of the annealed sheet increased. This was the combined effect of decreasing the dislocation density in the deformed microstructure and increasing the precipitate size.
- (3) The annealed sheet processed by direct cold rolling exhibited strong  $\eta$ -fiber texture and weak  $\{111\}\langle 112\rangle$  and  $\{001\}\langle 130\rangle$  texture. Hot rolling with 20% reduction obviously enhanced the  $\eta$  and Cube recrystallization texture. The magnetic induction at RD increased from  $\sim 1.74$  T to  $\sim 1.76$  T. When the hot rolling reduction reached 36–52%, enhanced  $\alpha$ -fiber recrystallization texture accompanied by a weakening of the  $\eta$  texture developed, resulting in a decrease in the magnetic induction.

**Author Contributions:** Conceptualization, H.J.; methodology, H.J. and L.Z.; validation, X.X., X.H. and D.L.; formal analysis, H.J., L.Z. and Y.T.; investigation, X.X., X.H. and Y.T.; resources, D.L. and Y.H.; data curation, H.J.; writing—original draft preparation, H.J.; writing—review and editing, R.D.K.M.; project administration, H.J. All authors have read and agreed to the published version of the manuscript.

**Funding:** The authors acknowledge support from the Open Project of Key Laboratory of Conveyance and Equipment (East China Jiaotong University), the Ministry of Education (KLCE2021-07), the Science and Technology Research Project of Jiangxi Provincial Department of Education (GJJ210653, GJJ200606), the National Natural Science Foundation of China (51965022) and the Natural Science Foundation of Jiangxi Province (20202BABL204046).

**Data Availability Statement:** Not applicable.

**Acknowledgments:** The authors at ECJTU are grateful to Raja Devesh Kuma Misra for his willingness to collaborate and contribute to meaningful discussion.

**Conflicts of Interest:** The authors declare no conflict of interest.

## References

1. Nakayama, T.; Honjou, N. Effect of aluminum and nitrogen on the magnetic properties of non-oriented semi-processed electrical steel sheet. *J. Magn. Magn. Mater.* **2000**, *213*, 87–94. [[CrossRef](#)]
2. Leuning, N.; Steentjes, S.; Heller, M.; Korte-Kerzel, S.; Hameyer, K. On the correlation of crystallographic macro-texture and magnetic magnetization anisotropy in non-oriented electrical steel. *J. Magn. Magn. Mater.* **2019**, *490*, 165485. [[CrossRef](#)]
3. Lee, K.M.; Park, S.Y.; Huh, M.Y.; Kim, J.S.; Engler, O. Effect of texture and grain size on magnetic flux density and core loss in non-oriented electrical steel containing 3.15% Si. *J. Magn. Magn. Mater.* **2014**, *354*, 1324–1332. [[CrossRef](#)]
4. Zhang, Y.X.; Lan, M.F.; Wang, Y.; Fang, F.; Lu, X.; Yuan, G.; Misra, R.D.K.; Wang, G.D. Microstructure and texture evolution of thin-gauge non-oriented silicon steel with high permeability produced by twin-roll strip casting. *Mater. Charact.* **2019**, *150*, 118–127. [[CrossRef](#)]
5. Qin, J.; Yang, P.; Mao, W.; Ye, F. Effect of texture and grain size on the magnetic flux density and core loss of cold-rolled high silicon steel sheets. *J. Magn. Magn. Mater.* **2015**, *393*, 537–543. [[CrossRef](#)]
6. Lee, K.M.; Huh, M.Y.; Lee, H.J.; Park, J.T.; Kim, J.S.; Shin, E.J.; Engler, O. Effect of hot band grain size on development of textures and magnetic properties in 2.0% Si non-oriented electrical steel sheet. *J. Magn. Magn. Mater.* **2015**, *396*, 53–64. [[CrossRef](#)]
7. Chang, S.K. Magnetic anisotropies and textures in high-alloyed nonoriented electrical steels. *ISIJ Int.* **2007**, *47*, 466–471. [[CrossRef](#)]
8. Sahoo, G.; Singh, C.D.; Deepa, M.; Dhua, S.K.; Saxena, A. Recrystallization behaviour and texture of non-oriented electrical steels. *Mater. Sci. Eng. A* **2018**, *734*, 229–243. [[CrossRef](#)]
9. Park, J.T.; Szipunar, J.A. Evolution of recrystallization texture in nonoriented electrical steels. *Acta Mater.* **2003**, *51*, 3037–3051. [[CrossRef](#)]
10. Sanjari, M.; Mehdi, M.; He, Y.L.; Hilinski, E.J.; Yue, S.; Kestens, L.A.; Edrissy, A. Tracking the evolution of annealing textures from individual deformed grains in a cross-rolled non-oriented electrical steel. *Metall. Mater. Trans. A* **2017**, *48*, 6013–6026. [[CrossRef](#)]
11. Mehdi, M.; He, Y.; Hilinski, E.J.; Kestens, L.A.; Edrissy, A. The evolution of cube  $\{100\} \langle 100 \rangle$  texture in non-oriented electrical steel. *Acta Mater.* **2020**, *185*, 540–554. [[CrossRef](#)]
12. Kim, K.M.; Kim, H.K.; Park, J.Y.; Lee, J.S.; Kim, S.G.; Kim, N.J.; Lee, B.J.  $\{100\}$  texture evolution in bcc Fe sheets—Computational design and experiments. *Acta Mater.* **2016**, *106*, 106–116. [[CrossRef](#)]
13. Zhang, L.W.; Yang, P.; Mao, W.M. Opposite relationship between orientation selection and texture memory in the deformed electrical steel sheets during  $\alpha \rightarrow \gamma \rightarrow \alpha$  transformation. *J. Mater. Sci. Technol.* **2017**, *33*, 1522–1530. [[CrossRef](#)]
14. Takajo, S.; Merriman, C.C.; Vogel, S.C.; Field, D.P. In-situ EBSD study on the cube texture evolution in 3 wt% si steel complemented by ex-situ EBSD experiment—From nucleation to grain growth. *Acta Mater.* **2019**, *166*, 100–112. [[CrossRef](#)]
15. Wang, L.T.; Deng, C.H.; Dong, M.; Shi, L.F.; Zhang, J.P. Development of continuous casting technology of electrical steel and new products. *J. Iron Steel Res. Int.* **2012**, *19*, 1–6. [[CrossRef](#)]
16. Maleki, A.; Taherizadeh, A.; Hosseini, N. Twin roll casting of steels: An overview. *ISIJ Int.* **2017**, *57*, 1–14. [[CrossRef](#)]
17. Li, J.; Sun, Y.; Zhao, Y.; Yu, X.-J.; Li, B. Effect of Al content on magnetic properties of non-oriented electrical steel by simulated CSP process. *J. Iron Steel Res.* **2007**, *14*, 364–367. [[CrossRef](#)]
18. Cong, J.; Guo, F.; Qiao, J.; Qiu, S.; Wang, H. Optimum magnetic properties of non-oriented electrical steel produced by compact strip production process. *Metals* **2022**, *12*, 64. [[CrossRef](#)]
19. Liu, H.; Liu, Z.; Li, C.; Cao, G.; Wang, G.D. Solidification structure and crystallographic texture of strip casting 3 wt.% Si non-oriented silicon steel. *Mater. Charact.* **2011**, *62*, 463–468. [[CrossRef](#)]
20. Wang, Y.; Zhang, Y.X.; Lu, X.; Fang, F.; Xu, Y.B.; Cao, G.M.; Li, C.G.; Misra, R.D.K.; Wang, G.D. A novel ultra-low carbon grain oriented silicon steel produced by twin-roll strip casting. *J. Magn. Magn. Mater.* **2016**, *419*, 225–232. [[CrossRef](#)]
21. Liu, Z.; Kobayashi, Y.; Yang, J.; Nagai, K.; Kuwabara, M. Effect of nano-scale copper sulfide precipitation on mechanical properties and microstructure of rapidly solidified steel with tramp copper element. *Mater. Trans.* **2006**, *47*, 2312–2320. [[CrossRef](#)]
22. Xu, Y.B.; Zhang, Y.X.; Wang, Y.; Li, C.G.; Cao, G.M.; Liu, Z.Y.; Wang, G.D. Evolution of cube texture in strip-cast non-oriented silicon steels. *Scr. Mater.* **2014**, *87*, 17–20. [[CrossRef](#)]
23. Jiao, H.T.; Xu, Y.B.; Zhang, Y.X.; Wang, Y.; Lu, X.; Fang, F.; Cao, G.M.; Li, C.G.; Wang, G.D. Effect of strip casting on magnetic anisotropy of non-oriented electrical steels. *Sci. Adv. Mater.* **2017**, *9*, 1822–1827. [[CrossRef](#)]
24. Sha, Y.H.; Sun, C.; Zhang, F.; Patel, D.; Chen, X.; Kalidindi, S.R.; Zuo, L. Strong cube recrystallization texture in silicon steel by twin-roll casting process. *Acta Mater.* **2014**, *76*, 106–117. [[CrossRef](#)]
25. Xu, Y.; Jiao, H.; Qiu, W.; Misra, R.D.K.; Li, J. Effect of cold rolling process on microstructure, texture and properties of strip cast Fe-2.6%Si steel. *Materials* **2018**, *11*, 1161. [[CrossRef](#)]
26. Liu, H.; Li, H.; Wang, H.; Liu, Y.; Gao, F.; An, L.; Zhao, S.; Liu, Z.; Wang, G. Effects of initial microstructure and texture on microstructure, texture evolution and magnetic properties of non-oriented electrical steel. *J. Magn. Magn. Mater.* **2016**, *406*, 149–158. [[CrossRef](#)]

27. Jiao, H.; Xu, Y.; Qiu, W.; Xu, H.; Misra, R.D.K.; Du, Y.; Li, J.; Wang, G. Significant effect of as-cast microstructure on texture evolution and magnetic properties of strip cast non-oriented silicon steel. *J. Mater. Sci. Technol.* **2018**, *34*, 2472–2479. [[CrossRef](#)]
28. Takatani, H.; Gandin, C.-A.; Rappaz, M. EBSD characterisation and modelling of columnar dendritic grains growing in the presence of fluid flow. *Acta Mater.* **2000**, *48*, 675–688. [[CrossRef](#)]
29. Rodríguez-Calvillo, P.; Houbaert, Y.; Petrov, R.; Kestens, L.; Colás, R. High temperature deformation of silicon steel. *Mater. Chem. Phys.* **2012**, *136*, 710–719. [[CrossRef](#)]
30. Humphreys, F.J.; Hatherly, M. *Recrystallization and Related Annealing Phenomena*, 3rd ed.; Elsevier: Amsterdam, The Netherlands, 2017; pp. 427–431.
31. Sakai, T.; Belyakov, A.; Kaibyshev, R.; Miura, H.; Jonas, J.J. Dynamic and post-dynamic recrystallization under hot, cold and severe plastic deformation conditions. *Prog. Mater. Sci.* **2014**, *60*, 130–207. [[CrossRef](#)]
32. Jiao, H.; Xu, Y.; Zhao, L.; Misra, R.D.K.; Tang, Y.; Liu, D.; Hu, Y.; Zhao, M.; Shen, M. Texture evolution in twin-roll strip cast non-oriented electrical steel with strong Cube and Goss texture. *Acta Mater.* **2020**, *199*, 311–325. [[CrossRef](#)]
33. Nguyen-Minh, T.; Sidor, J.J.; Petrov, R.H.; Kestens, L.A.I. Occurrence of shear bands in rotated Goss ( $\{110\}\langle 110\rangle$ ) orientations of metals with bcc crystal structure. *Scr. Mater.* **2012**, *67*, 935–938. [[CrossRef](#)]
34. Jenkins, K.; Lindenmo, M. Precipitates in electrical steels. *J. Magn. Magn. Mater.* **2008**, *320*, 2423–2429. [[CrossRef](#)]